ELSEVIER

Available online at www.sciencedirect.com

SCIENCE DIRECT®

Earth and Planetary Science Letters 215 (2003) 135–150

EPSL

www.elsevier.com/locate/epsl

Structure and evolution of the Molucca Sea area: constraints based on interpretation of a combined sea-surface and satellite gravity dataset

Christina Widiwijayanti[a,b,*], Valentin Mikhailov[c], Michel Diament[a], Christine Deplus[a], Rémy Louat[d], Sergei Tikhotsky[c], Alexei Gvishiani[c]

[a] *Laboratoire de Gravimétrie et Géodynamique, Département de Géophysique Spatiale et Planétaire (UMR CNRS/IPGP/P7 7096), Institut de Physique du Globe de Paris, Case 89, 4 Place Jussieu, 75252 Paris Cedex 05, France*

[b] *Research Center for Geotechnology, Indonesian Institute of Sciences (LIPI), Jl. Sangkuriang, Bandung 40135, Indonesia*

[c] *United Institute of Physics of the Earth, RAS, 3 Molodejnaya, Moscow 117964, Russia*

[d] *Institut de Recherche pour le Développement, 213 rue La Fayette, 75480 Paris Cedex 10, France*

Received 3 June 2002; received in revised form 12 June 2003; accepted 17 July 2003

Abstract

The paper presents an interpretation of the complete Bouguer gravity anomaly for the Molucca Sea area (northeast of Indonesia) in order to investigate the structure and interrelation of the main tectonic units of the region. Data on the gravity field and topography incorporate all available shipboard and satellite-derived data, including data collected during a 1994 R/V *L'Atalante* cruise in the Molucca Sea (MODEC). These data were compiled by weighted interpolation of surface and satellite data. The anomalous gravity field of the area contains components of different wavelengths, which we separated into regional and local anomalies using a spherical analogue of Kolmogorov–Wiener optimal (mean-square) filtering. Position and depth of the shallow lithospheric gravity sources were then estimated from the local field component by applying a new approach to Euler solution selection based on a recently developed fuzzy logic clustering method, called RODIN. The spatial distribution and depth of Euler solutions provide new information on the tectonic structure of the upper lithosphere resulting from the convergence of the Philippine Sea, Eurasian and Australian plates. The local Bouguer anomalies and dense clusters of Euler solutions make it easy to trace the Sangihe Trench further north, up to 5.5°N, joining it to the Pujada and Miangas ridges and to trace the Miangas Ridge southwards to its junction with the Central Ridge. Seismic data revealing compressive structure and dense shallow clusters of Euler solutions suggest that the Pujada Ridge overthrusts the Miangas Ridge from the west. Clusters of Euler solutions also clearly outline an ophiolite body of the Talaud Archipelago, show main thrust zones bounding it, and trace the southern termination of the Philippine Fault horsetail structure up to 5.5–6°N in the area southeast of Mindanao Island. Our results support the hypothesis that the Talaud Archipelago was formed in situ as an uplifted Central Ridge block. We suggest that the structure of the Archipelago and of the area to the east

---

* Corresponding author. Tel.: +33-1-44-27-7345; Fax: +33-1-44-27-7340.
E-mail address: widiwij@ipgp.jussieu.fr (C. Widiwijayanti).

doi:10.1016/S0012-821X(03)00416-3

developed under compression caused by docking of the Snellius Plateau. The docking shifted the Philippine subduction zone eastwards and underthrust slivers of forearc lithosphere below the Talaud Archipelago.

Keywords: gravity field; Molucca Sea; crustal structure; geodynamics; Euler deconvolution

1. Introduction

The Molucca Sea, located between the East Indonesian and the Philippine archipelagos, is probably one of the most complicated tectonic areas in Southeast Asia. The Molucca Sea Plate, now almost completely subducted, is squeezed between the converging Philippine Sea, Eurasian and Australian plates (Fig. 1). The overall tectonic setting has been studied using numerous geophysical and geological data ([1–13] and many others), but many details are still unclear. In particular, the northward continuation of the Molucca Sea subduction zones, the southern propagation of the Philippine Fault, and the structure and origin of the Snellius Plateau remain controversial (Fig. 1).

To investigate peculiarities of the upper lithospheric structure of the region, we compiled a new complete Bouguer anomaly dataset using all available shipboard and satellite data. We then applied a 3-D separation technique [14] to extract the signal caused by shallow lithospheric sources. To estimate the shape and depth of possible causative bodies, we applied a recently introduced artificial intelligence technique for the Euler solution selection [15]. Finally, we combine the results of this analysis with other available data to investigate the main subsurface structural features and constrain geodynamics of the region.

2. Tectonic settings

Located in a convergent zone between three plates, the Molucca Sea is characterized by a complicated melange of tectonic structures (Fig. 1). The sophisticated combination of subduction zones bounding the sea incorporates two oppositely dipping sides of the Molucca Sea Plate, the Philippine subduction zone to the east and the Cotabato subduction zone to the west (Fig. 1). Most of the Molucca Sea convergence is accommodated by a double-verging subduction of the Molucca Sea lithospheric plate: westward subduction beneath the Sangihe Arc (Eurasian margin) and eastward subduction beneath the Halmahera Arc (a fragment of the Philippine Sea Plate) [1,4,5]. Convergence of these arcs led to collision, so the area between the two arcs is now filled with strongly deformed units of varying lithologies, previously termed the melange wedge [1] or collision complex [4]. These deformed units cover both Molucca Sea trenches, being obducted onto the flanking arc (Fig. 1). Seismic refraction profiles running across the southern Molucca Sea reveal a low velocity body more than 15 km thick [6,7], which is the source of a large negative gravity anomaly.

A tectonic melange including ophiolite blocks exposed on the Talaud Archipelago and the Mayu and Tifore Islands is interpreted as slivers of oceanic crust and trench sediments uplifted in the forearc terrain [8,9]. These islands form a ridge that bisects the collision complex and generates a free-air gravity anomaly high [6,10]. Ophiolitic rocks cropped on the islands are thought to represent slices of the Molucca Sea crust that overthrust the collision complex (e.g. [8,9]). The Talaud islands are attributed either to an uplifted part of the active collision complex [2,6], to the northern limit of the forearc terrain of the Halmahera arc system [3,7], or to the outer ridge of the Sangihe subduction zone [10,11].

North of the Talaud Archipelago, in the Mindanao Island region, the convergence manifests itself in a different structural style [2,4]. Here, oblique convergence of the Philippine Sea Plate generates left-lateral strike-slip movement along the Philippine Fault [1]. The southward termination of the fault is observed offshore of Mindanao as a horsetail structure [12]. The position and origin of many structures of the area remain contro-

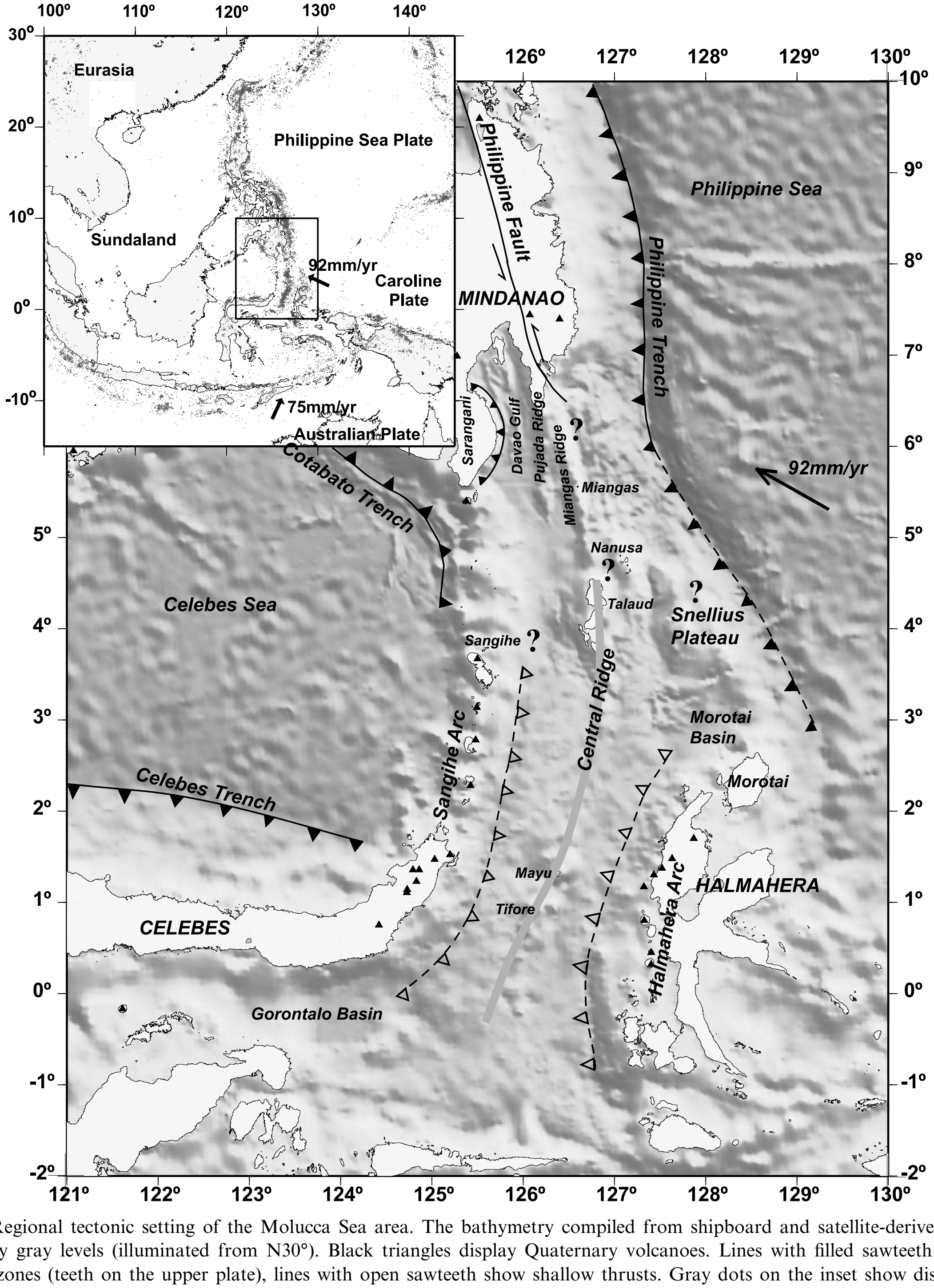

Fig. 1. Regional tectonic setting of the Molucca Sea area. The bathymetry compiled from shipboard and satellite-derived data is shown by gray levels (illuminated from N30°). Black triangles display Quaternary volcanoes. Lines with filled sawteeth are subduction zones (teeth on the upper plate), lines with open sawteeth show shallow thrusts. Gray dots on the inset show distribution of shallow (<60 km) seismicity according to the EHB 1964–1999 catalogue [24]. Epicenters clearly outline boundaries of the plates. The arrows represent the convergence of the Philippine Sea Plate and Australian Plate relative to the Eurasia Plate [25,26]. Study area is marked by the rectangle in the inset.

versial. According to Rangin et al. [11], the Snellius Plateau, which is considered to be the northern extension of the Halmahera Arc, underthrust Talaud, causing its uplift. Another tectonic scheme [13] suggests that the Sangihe trench continues northward up to east of Miangas. Hence, the Central Ridge could be a backstop of the Sangihe subduction zone [10].

3. Data collection and processing

3.1. Complete Bouguer gravity anomaly

The free-air gravity anomaly dataset for the study area was compiled using data from the 1994 MODEC marine survey [11] in the Molucca Sea area (ship tracks are shown in Fig. A2 of Appendix 1) and available marine gravity data from the NOAA National Geophysical Data Center (NGDC). As marine gravity data do not provide uniform coverage of the study area, we combined them with satellite altimetry-derived gravity data compiled by KMS [16] (for more information on the comparison of shipboard and satellite gravity data, see Appendix 1). A combined $1' \times 1'$ dataset was obtained by interpolating shipboard data with KMS grid points situated outside $5'$ (about 9.3 km) vicinity of the ship tracks. A bigger weight was given to the shipboard data. Such processing retains the higher resolution of the surface data while taking advantage of the uniform satellite coverage. We used a similar procedure to combine the swath bathymetry data collected during the MODEC cruise with other NGDC bathymetry data and the satellite-predicted bathymetry of Smith and Sandwell [17].

The bathymetric grid was used to calculate the gravity effect of the seafloor topography, assuming the water and crustal density to be 1030 and 2680 kg/m^3 respectively and keeping four terms in Parker's formula [18]. As the topography of the study area is highly variable we fixed the reference level at a water depth of 4000 m to reduce the edge effect. The spatial distribution of marine gravity surveys allows the computation of a complete Bouguer dataset at $1' \times 1'$ grid (approximately 1.85 km). Such a grid spacing is sufficient to represent gravity sources of 10–15 km horizontal dimension.

Simple visual inspection of the complete Bouguer anomaly map (Fig. 2) shows that the anomaly field contains at least two components of considerably different wavelengths. The long wavelength (regional) component reveals first order tectonic features. Positive anomalies clearly outline the oceanic lithosphere of the Philippine and Celebes Sea plates. A linear, roughly north–south trending negative anomaly mainly follows the Central Ridge. To the South of Talaud, this anomaly is much wider than the topographic high and covers the strongly deformed accretionary wedges located on the both sides of the Ridge. Further to the north, close to Mindanao this anomaly follows the eastern flank of the topographic high and is shifted toward the Philippine Trench.

At a more local scale (short wavelength), the relations between the tectonic structure and the gravity signature are less clear, being partly masked by the strong regional component. As our study was aimed to investigate the upper lithospheric structure of the region, and assuming that the short wavelength (local) component mostly reflects shallow crustal structures, position of suture zones, faults, etc., we first faced the problem of separating these two components. We performed this using a spherical analogue of the Kolmogorov–Wiener optimal filter developed by Gordin et al. [14].

3.2. Separation of gravity anomalies into regional and local components

The basis of separation technology is described in the following analogy between the equivalent sources technique and Kolmogorov–Wiener optimal filtering [14]. Let us assume a gravity anomaly is the sum of two uncorrelated components of different wavelength. We represent the regional component by a cumulative gravity field of a set of elementary sources (e.g. point masses or dipoles), situated below the data points at some depth h_{reg}. The local component can be represented as a gravity field of another set of sources located in the same horizontal positions, but at a

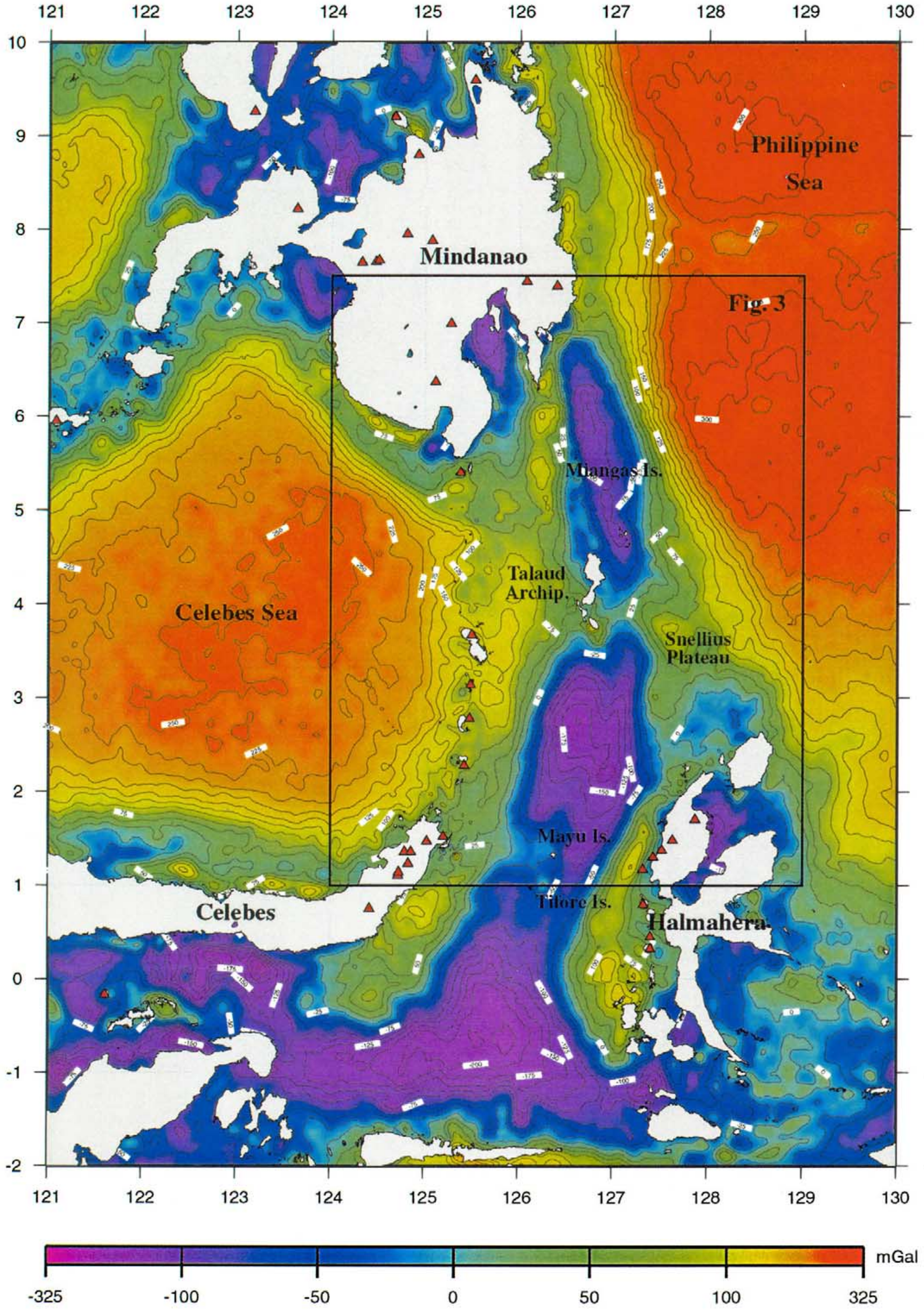

Fig. 2. Complete Bouguer anomaly of the Molucca Sea area shown by color levels and isolines. Rectangular box shows location of Fig. 3. Triangles display Quaternary volcanoes.

shallower depth h_{loc}. The source masses are defined from the equivalence of the total model field to the given one. If: (i) the autocorrelation function of each component is equal to the gravity field of elementary source situated at corresponding depth, and (ii) the ratio of masses of the two sources situated below every data point is constant and equal to the ratio of the root-mean-square amplitudes of the corresponding signal components, then the procedure of the described equivalent sources approximation is identical to those of Kolmogorov–Wiener optimal filtering [14,19]. A detailed description is given in Appendix 2. This analogy allows us to extend very efficient (e.g. for calculation of directional derivatives, reduction, etc.) equivalent source techniques to the case of multi-source systems representing different field components.

When separating a field into two components, three free parameters have to be assigned: the two radii of autocorrelation of each signal and the ratio of their root-mean-square amplitudes. The separation quality depends on how different the spectral characteristics of the signals are and on the proper choice of parameters of separation. Fortunately, the Molucca Sea dataset is very favorable for separation, as even from simple visual inspection it is clear that the Bouguer gravity field contains two components. The regional component has a characteristic wavelength of several hundred kilometers, while the wavelength of the local component is at least one order of magnitude smaller. Because the regional component correlates well with regional tectonic features such as lithospheric plates, subduction zones, sedimentary wedges, etc., its causative sources are most probably situated at different depths in the lithosphere and in the upper mantle below. In contrast, the causative sources of the short wavelength local component, assuming reasonable density contrasts, are situated mainly at a relatively shallow depth (in the upper lithosphere). This component depicts tectonic features such as crustal-scale thrusts, faults, small sedimentary basins, etc. Further we consider only the local component.

The parameters of separation (i.e. parameters of equivalent sources) can be estimated by calculating the autocorrelation function or power spectral density of the given gravity field [20], or simply by visual inspection of the field, as the characteristic dimensions of the gravity anomalies representing the two components are clearly linked to the depth of equivalent sources (for more discussion and synthetic and real examples see [14,20]). In our study we used both approaches. We also ran calculations for different parameter values, analyzing the smoothness of the regional field and the low correlation of regional and local components using maps and a system of cross-sections. These calculations demonstrated that the final results are stable for up to 10% variations in the separation parameters. Using this approach we estimated the depth to the equivalent sources as $h_{reg} = 240$ km and $h_{loc} = 60$ km, and the ratio of the root-mean-square amplitudes of the regional and local components as 3.5.

The regional component looks similar to the total Bouguer anomaly (Fig. 2) because the amplitude of the long wavelength component is considerably larger than that of the local component. The main features better imaged by the regional component are: isometric positive anomalies inside the Celebes Sea Plate, a gravity low separating the Philippine Sea Plate at latitude 8°N and positive gravity anomaly extending to the east of the Sangihe volcanic arc. In its southern part this anomaly clearly follows the Sangihe Trench, enabling us to trace it up to 5.5°N, where it connects to the Pujada Ridge.

The local Bouguer anomaly component (Fig. 3) better outlines the shallow short wavelength structures. A strong positive anomaly follows the bathymetric high joining ophiolite outcrops of the Mayu-Tifore and Talaud Ridge [6–10] and permits one to trace the Central Ridge up to its approach to the Pujada and Miangas ridges. This anomaly is bordered on both sides by local negative anomalies, which outline low density material of highly deformed accretionary bodies, in particular a thick accretionary wedge to the east of the Miangas Ridge [10]. The local Bouguer anomaly map also outlines the Halmahera Trench up to 2°N, following the trace of the Halmahera volcanic arc. The Sangihe volcanic arc at the western boundary of the Molucca Sea is outlined

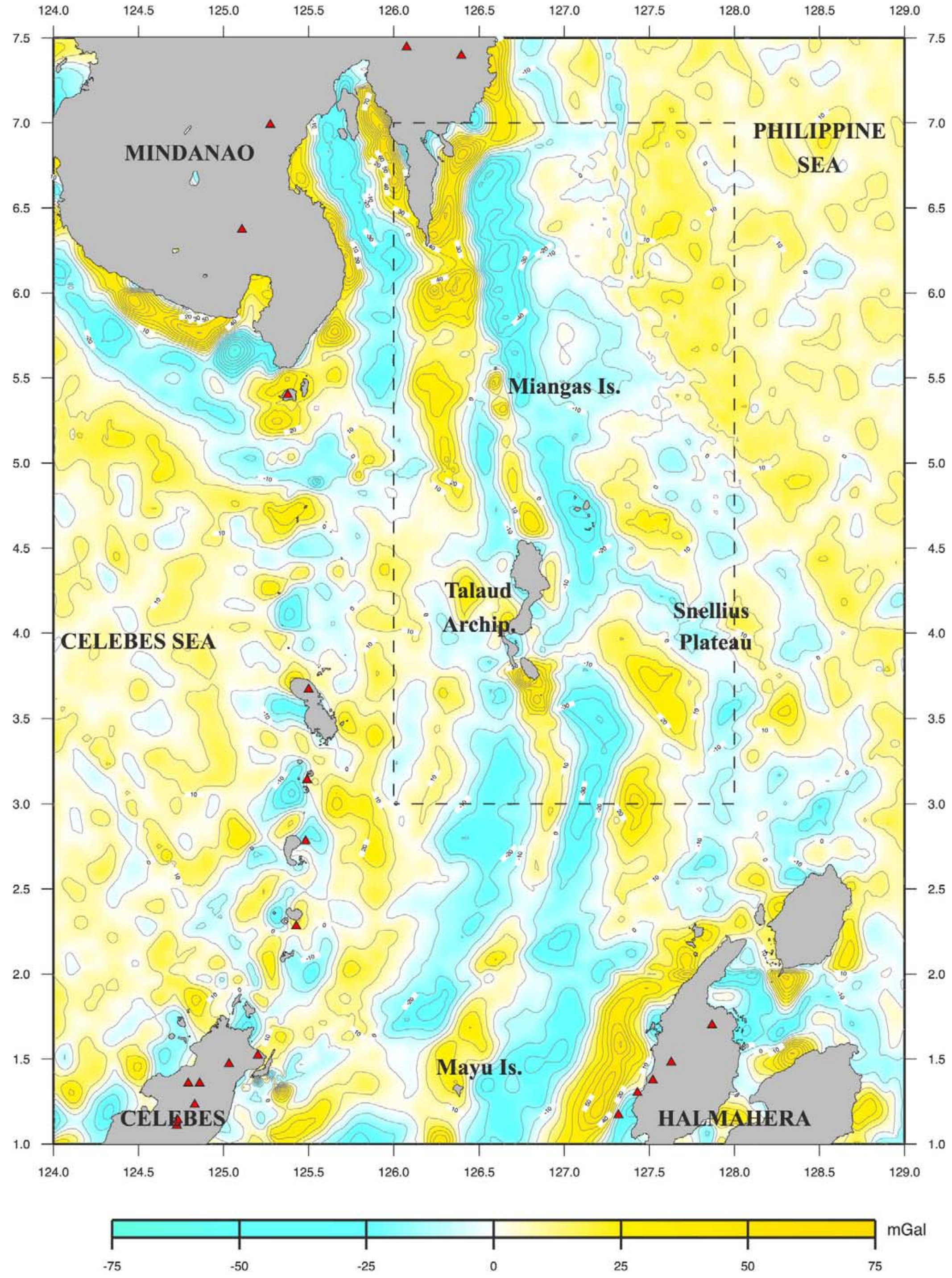

Fig. 3. Local component of the Bouguer anomaly. Positive anomalies are shown by yellow color levels and negative anomalies shown by green levels. The dashed line shows the area of Fig. 4.

by negative local Bouguer anomalies, and the Talaud Archipelago is mostly bounded by a gravity high.

The central part of the Snellius Plateau is represented by a local negative anomaly presumably caused by low density crustal material forming the Plateau. The local field amplitude in the Plateau area should be treated with caution, as weak local anomalies of 10–20 mGal were registered over the background regional anomaly level of more than 200 mGal. Nevertheless, the local anomalies clearly outline main structural axis of the area.

To interpret the local component of the Bouguer anomaly we employed the recent modification of the Euler deconvolution method [15] based on a new clustering method [21].

3.3. Interpretation of the local gravity anomalies

The idea of Euler deconvolution is to approximate a measured anomaly in a running window by the field of some elementary source of uniform density or magnetization. The position of elementary sources (so-called Euler solutions) often characterizes the location and/or contour of causative bodies and provides some estimate on their depth. It is especially true for isolated restricted causative bodies. The method has two free parameters: the size of the running window and the so-called structural index, which determines which type of elementary body to use for the approximation (e.g. a point pole, dipole, line of masses, etc.). It also routinely includes selection of Euler solutions [22], rejecting ones with low tolerance, large dispersion of depth estimates, or with depths that are unreasonably shallow or deep. In the regions of complicated tectonic structure, where anomalies are caused by multiple sources including structural interfaces and compact bodies of different size and depth, the method does not always provide easily interpretable results. Nevertheless, even if Euler solutions form broad clouds, making it difficult to constrain causative sources, the densest aggregations of Euler solutions cluster around centers of mass or contours of causative bodies. Mikhailov et al. [15] suggested using a clustering technique to serve as a tool for selecting appropriate solutions and demonstrated its efficiency in revealing causative bodies on synthetic and real examples.

We used a clustering method, called RODIN [21], that is based on a new formal mathematical definition of a cluster as a subset in a finite metric space. RODIN depends on free parameters that facilitate the search for clusters, following given set of properties. Thus, the procedure employed includes three consequent steps. The first step consists of the calculation of Euler solutions [22]. At this step two parameters have to be assigned: the width of the running window and the structural index. At the second step, convenient methods of Euler solution selection can be applied. In the third step, an additional selection is made using the RODIN clustering algorithm. The results of this step depend on two parameters: one controlling the quality (density) of clusters and another one controlling the shape of clusters, permitting selection of more isometric or elongate ones. All the parameters have simple meanings and their influence on the final solution is clear. The RODIN software also possesses visualization tools allowing interactive controlling of parameter choice at every step. The choice of parameters in this approach cannot be considered a difficult problem.

The results of Euler deconvolution without the clustering technique for the central part of the study area (marked by the dashed line in Fig. 3) with structural index 2 (point mass) and window size 25′×25′ are presented in Fig. 4A. Even using different criteria for Euler solution selection, the result does not provide useful constraints on the tectonic structure. Application of clustering technique considerably reduces the number of solutions and permits the identification of dense clusters, which depict main causative bodies in the region (Fig. 4B).

3.4. Stability of the results of gravity field interpretation

Before considering the result of gravity field interpretation, it is worthwhile emphasizing again that in this study we restrict our consideration to the local component of the gravity field. This component depicts more clearly low amplitude

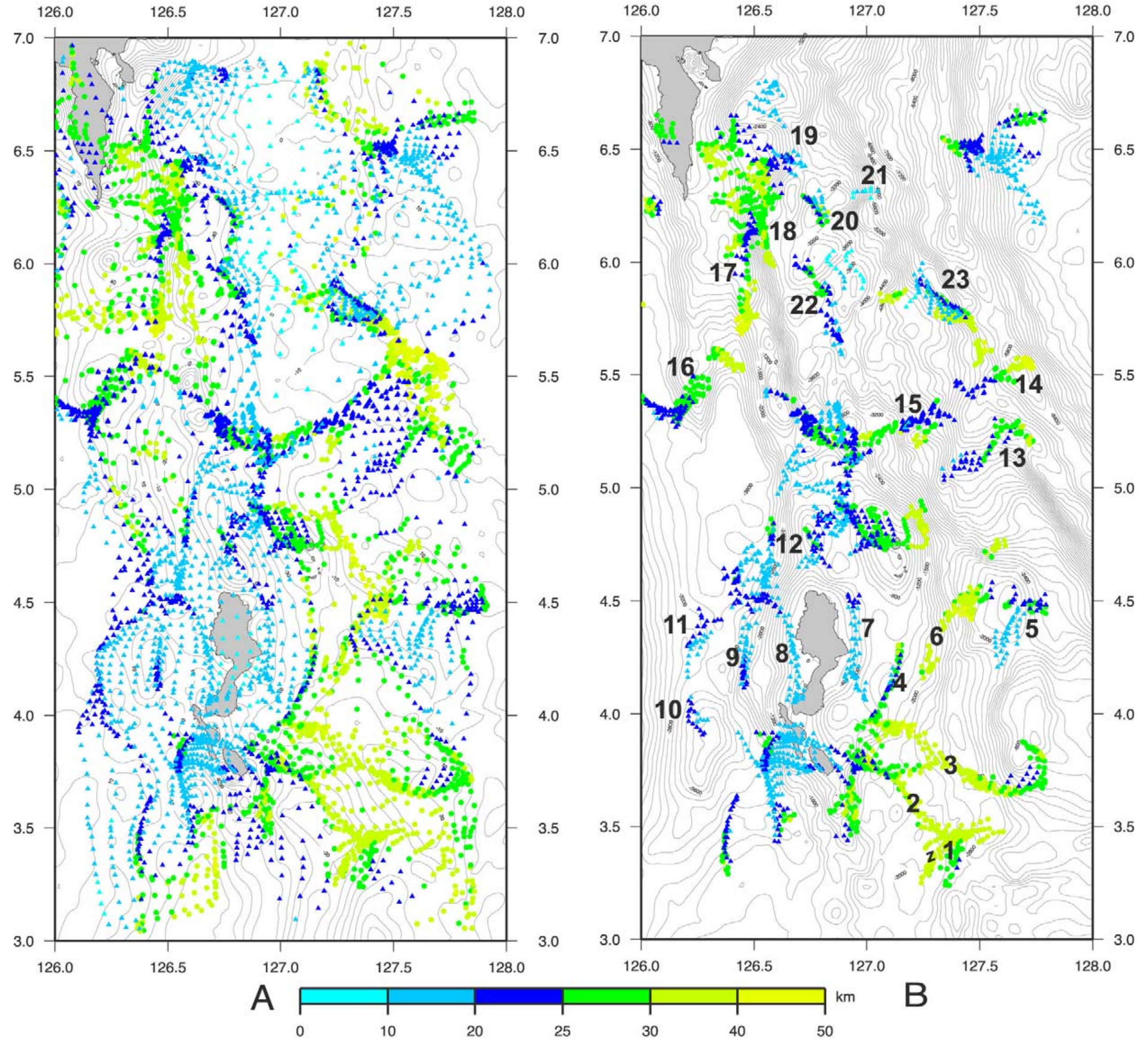

Fig. 4. Euler solutions obtained from the local component of the Bouguer anomaly. Shallow solutions (0–25 km) are shown by blue triangles, deeper ones (25–50 km) by green and yellow dots. (A) Solutions selected using standard criteria [22] shown on the background of the local Bouguer anomalies. (B) Solutions selected by clustering technique [15] shown on the background of bathymetry. Numbers mark clusters discussed in the text.

short wavelength variations. All of these local features can be found on the map of the complete gravity field although less prominently (Fig. 2). Thus, it is easy to check that the analyzed features are not artefacts produced by field separation. In this case, the results of Euler deconvolution are not very sensitive to the parameters of separation. Indeed, for the Euler deconvolution we used a relatively small window (25′×25′, i.e. 46×46 km). In every window we determined not only the three coordinates of the Euler solution but also a constant field level (see [15]). Because the regional component is almost constant within these small windows, it does not significantly influence the results of the Euler deconvolution.

4. Discussion

Fig. 4B demonstrates that the clusters extend in several preferred directions. The deep solutions (25–50 km depth, shown by green and yellow dots in Fig. 4B) mainly form an orthogonal system, parallel (clusters 2, 3, 23 in Fig. 4B) or normal (clusters 1, 4–6, 13–15) to the direction of Philippine Sea Plate convergence. In the center of the area, shallow solutions (less than 25 km, shown by blue triangles) extend mainly in the north–south direction. Around the Talaud Archipelago shallow clusters (nos. 7, 8) outline the external boundary of the ophiolite body, exposed on the islands of the Central Ridge [7–10,23]. Sharp dense clusters apparently depict faults contouring the archipelago on all sides (Fig. 4B). We suggest that these faults were formed during uplift of the Sangihe forearc and the Central Ridge, which later formed the Talaud Archipelago. Clusters extending in the north–south direction west of Talaud (nos. 9, 12) trace intensive backthrusts shown in Fig. 5. Parallel to them a group of clusters situated further to the west (nos. 10, 11) follow the Sangihe Trench. These clusters coincide with the positive local Bouguer anomaly (Fig. 4).

North of the Archipelago, north–south trending clusters split into two branches. The western deeper ones (clusters 16, 17) depict a boundary between the Pujada and Miangas ridges. In light of seismic profiles [3,7,11] that reveal compressive structures to the west of the Pujada Ridge, one can suggest that this ridge itself overthrust the Miangas Ridge. Thus, the Euler solutions forming this cluster may outline the thrust front (Fig. 5). A deep north–south striking cluster (no. 18) continues eastwards of the Miangas Ridge. Focal mechanism solutions from the Harvard CMT catalogue suggest that this boundary probably follows a left-lateral strike-slip fault lying parallel to the Philippine fault (Fig. 5).

Shallower north–south clusters (no. 22) of direction striking continuously at the east from the Central Ridge possibly follow a structural boundary in the basement below the accretionary wedge. Several shallow clusters (nos. 19–21, 23) apparently depict the southern extension of the Philippine Fault, which separates into several branches in the north–south and northwest–southeast direction (Fig. 5).

To the east of Talaud there are two groups of deep clusters: one trending in a northeasterly direction (nos. 1, 4–6) and the other in a northwesterly direction (nos. 2, 3) (Fig. 4B). Clusters 2 and 3 extend from Talaud to the SW border of the Snellius Plateau and to a zone of crustal deformation northwest of the Morotai Basin (for the location see Fig. 1), suggesting that the formation of the archipelago was closely linked to the arrival of the Snellius Plateau. The present-day position of the Philippine Plate subduction zone is marked by a line of negative (on the overriding plate) and positive (on the approaching plate) local Bouguer anomalies (Fig. 3). Similarly, a north–south trending negative anomaly between Talaud and the Snellius Plateau that is bounded from the east by positive anomalies probably follows the southward continuation of the Philippine Plate subduction zone before its shift to the east after the Snellius Plateau arrived.

Thus, main tectonic features of the area can be explained by docking of the Snellius Plateau [11]. After the plateau approached the Philippine trench (as a part of the Halmahera Plate or as a separate terrain) it overrode the subduction zone and pushed the forearc lithosphere in front of it to the northwest. This sliver of forearc lithosphere underthrust and uplifted the Central Ridge block forming the Talaud Archipelago. As the Philippine Sea Plate continued to converge, the subduction shifted to the east of the Snellius Plateau. Deep clusters 2 and 3 to the east of Talaud correspond to the side boundaries of the underthrusting forearc plate. The line of deep clusters (no. 4) located close to Talaud corresponds to the back edge of the overthrusting plate or backthrust in the accretionary wedge (Fig. 5). The stretched shape of clusters 2–4 suggests that docking of the Snellius Plateau was likely accompanied by clockwise rotation.

Clusters 5, 6, and 13–15, situated further to the north, also apparently reflect thrusts formed as the result of docking of the Snellius Plateau and the eastward shifting of the subduction zone. Shallow cluster 5 in the northern part of the plateau presumably depicts a backthrust formed as

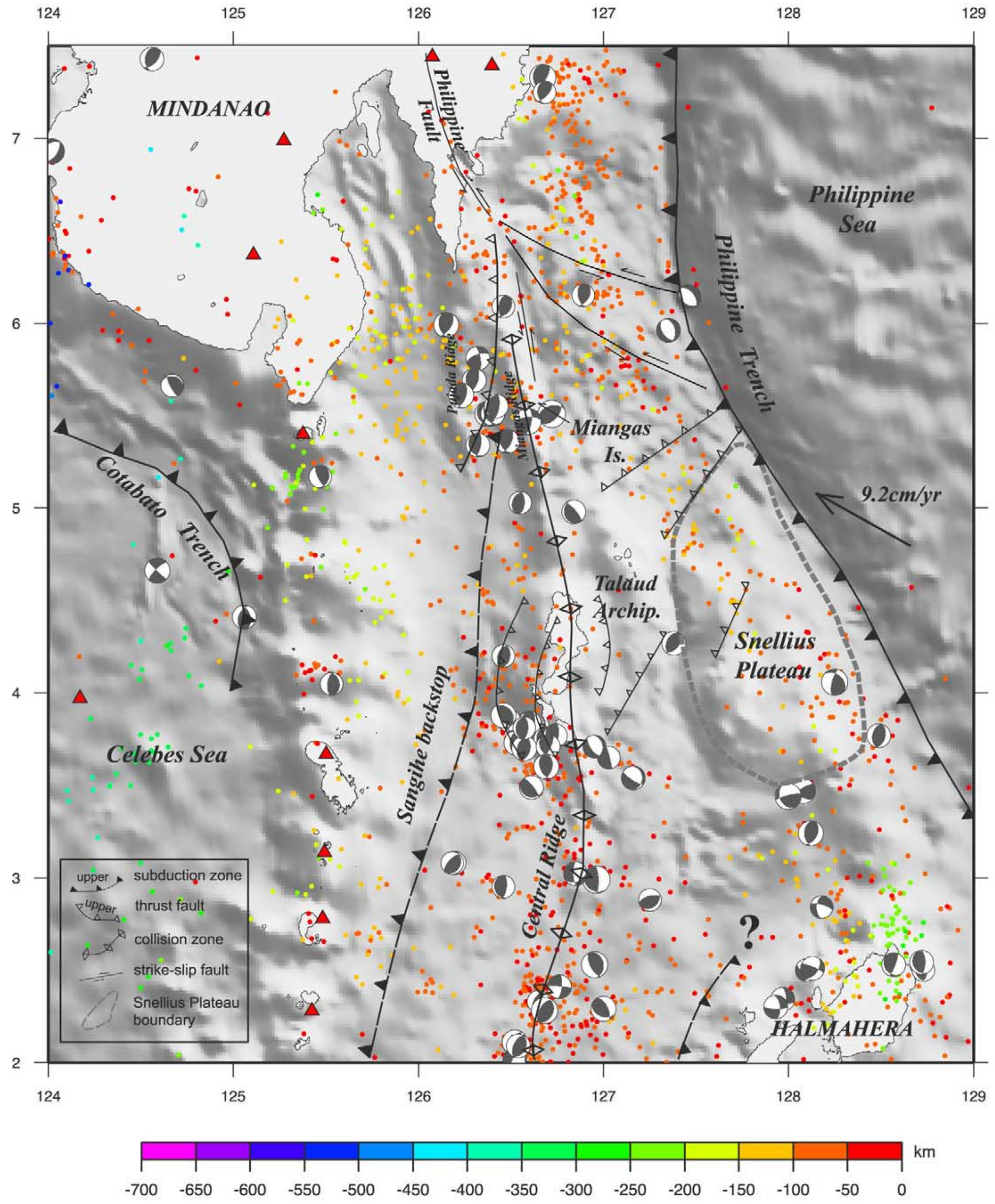

Fig. 5. Tectonic scheme of the area based on results of interpretation of compiled shipboard and satellite gravity dataset. Bathymetry is shown by gray scale. Depth of hypocenters is shown in colors (EHB catalogue [24]). Selected focal mechanism solutions according to Harvard CMT solutions catalogue are given for Mb > 5.5. Other symbols as in Fig. 1.

the result of northwest propagation of the Snellius Plateau. This may explain why this part of the plateau is characterized by a positive Bouguer anomaly.

5. Conclusions

We propose a consistent scheme for the structure and development of the Molucca Sea area based on the results of our detailed gravity dataset interpretation. Its main points are:

- The local structure of the Talaud Archipelago and the area to the east agrees with the hypothesis that the Snellius Plateau arrived at the Philippine subduction zone (e.g. [11]). The subduction was repositioned eastwards because the plateau overrode the trench. We suggested that north–south trending negative anomalies between Talaud and Snellius Plateau bounded from the east by positive anomalies (Fig. 3) outline the former position of the subduction zone south of 5–6°N. As a consequence, the different trends and depths of the Philippine Trench north and south of 5–6°N do not result from southward trench propagation (cf. [13]) but from eastward shift of the subduction zone.
- Dense Euler solution clusters depict thrust faults bounding the Talaud Archipelago, suggesting that the archipelago is not a terrain, as suggested by [7], but an uplifted Central Ridge block. We suggest that the uplift of this block resulted from northwestward compression caused by the docking and probable clockwise rotation of the Snellius Plateau terrain.
- The local Bouguer anomalies clearly show that the Sangihe Trench (forearc) extends north up to 5.5°N, where it joins the Pujada and Miangas ridges [10]. The Pujada Ridge presumably overthrusts both the forearc and the Miangas Ridge located to the east.
- The southern extension of the Philippine Fault as a horsetail structure can be traced offshore far to the southwest of Mindanao, as far as 5.5–6°N.

Our approach appears to be a very efficient method for studying upper lithosphere structure and geodynamics by combining surface and satellite gravity data. Data from forthcoming high resolution satellite missions, e.g. GOCE, will allow its further development and application to regions which are presently poorly served.

Acknowledgements

We thank the captain and crew of the MODEC 1994 R/V *L'Atalante* cruise for their efficient work at sea and the scientific party for the data and fruitful discussions. The very constructive comments of M. Pubellier and an anonymous reviewer greatly improved the manuscript. We also thank A. Cazenave and W. Crawford for their comments. Most of the figures were prepared using the GMT software developed by P. Wessel and W. Smith. C.W. benefited from a grant from the Ministére des Affaires Etrangères (France) and from IRD during this study. This research is a result of IPGP-UIPE collaboration. The paper is IPGP contribution No. 1929.***[AC]***

Appendix 1. Comparison between shipboard and satellite-derived gravity data in the Molucca Sea area

In our study we compared shipboard data obtained during the MODEC 1994 cruise with two satellite-derived models of the Earth's gravity field: the KMS 1998 model of Andersen and Knudsen [16] and the SS92 model (version 9.2) of Sandwell and Smith [27]. Satellite-derived models provide uniform coverage of the Earth's surface, but do not detect very short wavelength structures. The resolution of these models can be improved by combining them with available surface (in our case shipboard) data, which are more precise at a short wavelength.

We present results of a detailed comparison of shipboard data obtained during the MODEC 1994 cruise with the two satellite gravity models. In general, the three datasets are close, with the KMS 1998 model better fitting the shipboard data, especially close to shorelines (see Fig. A1). Discrepancies between the satellite gravity models could result from the different numerical algo-

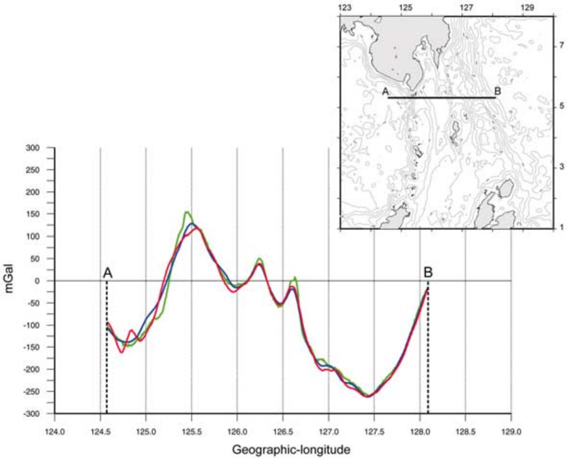

Fig. A1. Comparison of MODEC 1994 cruise data (green line) with satellite-derived gravity field of Sandwell and Smith, version 9.2 [27] (red line) and KMS 1998 [16] (blue line) along one east–west MODEC ship track (see inset for location).

rithm used to calculate them. Fig. A1 presents a comparison of the three datasets along one ship track running east–west.

The results of a statistical analysis of model discrepancies is given in Table A1. These results confirm the better agreement of the MODEC 1994 and KMS 1998 data.

Fig. A2 shows the spatial distribution of differences between the MODEC 1994 and KMS 1998 data. It is clearly seen that the main errors occur close to the shorelines, where satellite altimetry data are less precise. A procedure to improve resolution of satellite models close to the shorelines is discussed in [28].

Based on results of the satellite model comparison, we chose to combine the KMS 1998 model with the MODEC 1994 and other shipboard data.

Appendix 2. Method of the gravity field separation

Consider the measured gravity anomaly $g(p_i)$, given at a set of points $\{p_i\}$, $i = 1, 2, ..., N$ at the Earth's surface. Let it consist of two components $g(p_i) = g_{\text{reg}}(p_i) + g_{\text{loc}}(p_i)$, that is the regional and local components. In the optimal filtration approach both components are assumed to be realizations of stationary and ergodic random processes. Normalized isotropic auto-correlation functions of these processes $R_{\text{reg}}(r) = \mathbf{M}[g_{\text{reg}}(\xi)\, g_{\text{reg}}(\xi + r)]/\sigma^2_{\text{reg}}$ and $R_{\text{loc}}(r) = \mathbf{M}[g_{\text{loc}}(\xi) g_{\text{loc}}(\xi + r)]/\sigma^2_{\text{loc}}$ are assumed to be known, where $\mathbf{M}[...]$ is the expectation operator, r is the distance along the Earth's surface between points; and σ^2_{reg} and σ^2_{loc} are the dispersions of the regional and local components (assumed uncorrelated).

Following the Kolmogorov–Wiener optimal filtering method [29,30], one obtains the optimal (in the least squares sense) estimation of the component g_{reg} at point p_j by weighted summation (the discrete analogue of convolution):

$$\tilde{g}_{\text{reg}}(p_j) = \sum_k w_{kj} \cdot g(p_k) \qquad (1)$$

where the vector of weights $\overline{w} = \{w_{kj}\}$ satisfies the equation:

$$\overline{R}_{\text{reg},j} = (\mathbf{R}_{\text{reg}} + \alpha^{-1}\mathbf{R}_{\text{loc}})\overline{w}_j \qquad (2)$$

The vector and matrices in Eq. 2 are composed of values of auto-correlation functions of both components: of the vector $\overline{R}_{\text{reg},j}$ are $\{R_{\text{reg}}(r_{jk})\}$, where r_{jk} denotes the distance between points j

Table A1
Statistical characteristics of the gravity datasets along the MODEC shipboard tracks

Input data	Mean value (mGal)	S.D. (mGal)	Minimum value (mGal)	Maximum value (mGal)	RMS difference to MODEC data	
					Mean (mGal)	S.D. (mGal)
MODEC cruise	−40.72	106.62	−281.00	210.00	0.00	0.00
Sandwell and Smith v. 9.2	−35.87	110.46	−288.00	206.20	−4.85	24.64
KMS 1998	−38.67	103.80	−276.80	192.60	−2.06	16.49

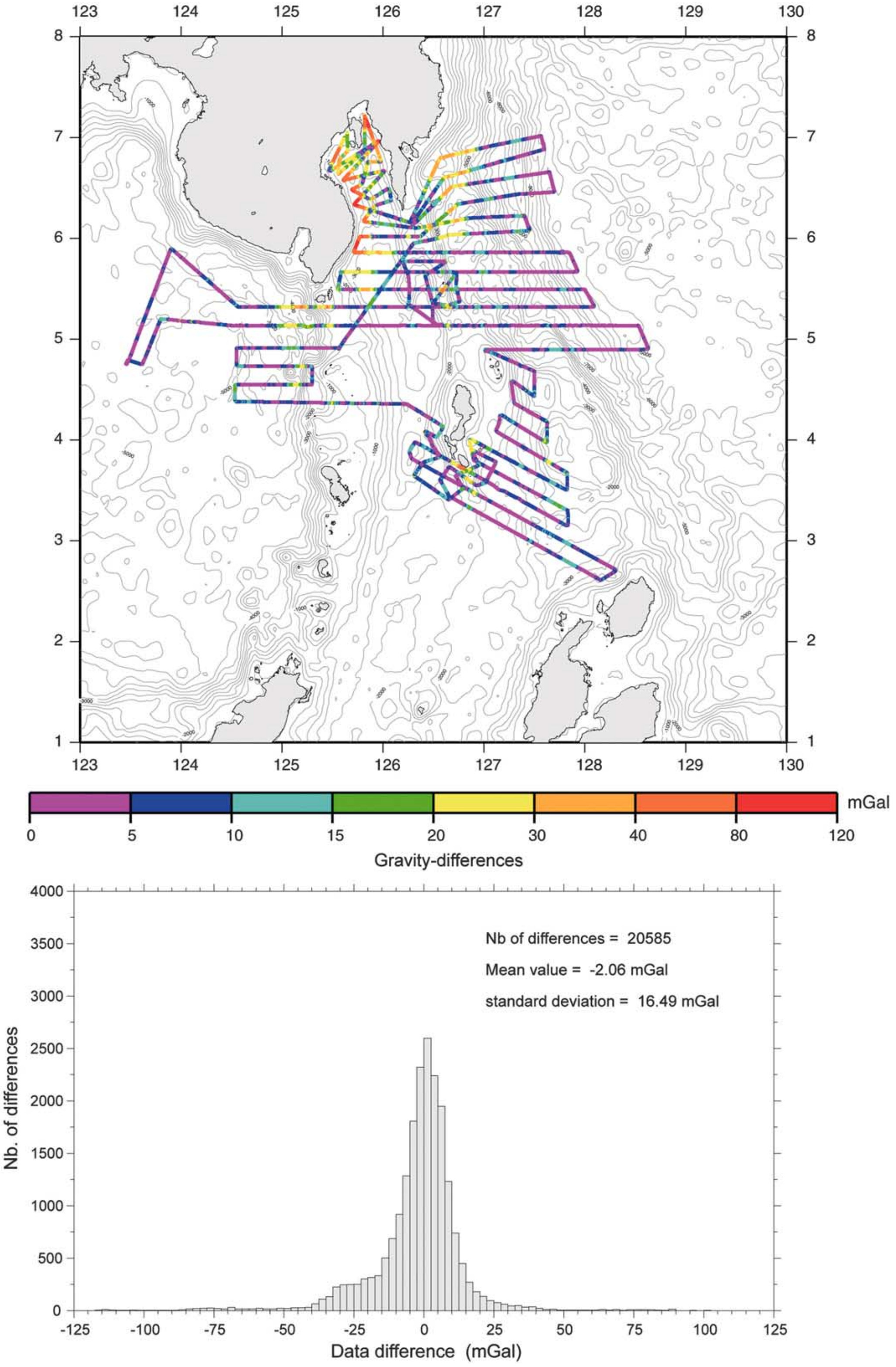
123
124
125
126
127
128
129
130
8
7
6
5
4
3
2
1
0
5
10
15
20
30
40
80
120
mGal
Gravity-differences
Nb of differences = 20585
Mean value = -2.06 mGal
standard deviation = 16.49 mGal
Nb. of differences
4000
3500
3000
2500
2000
1500
1000
500
0
-125
-100
-75
-50
-25
0
25
50
75
100
125
Data difference (mGal)

and k along the Earth's surface and the components of matrices are $\mathbf{R}_{reg} = \{R_{reg}(r_{ik})\}$ and $\mathbf{R}_{loc} = \{R_{loc}(r_{ik})\}$. The value $\alpha = \sigma^2_{reg}/\sigma^2_{loc}$ represents the 'signal-to-noise' ratio. In all the formulas the index j is fixed at the point p_j, for which the value $\overline{g}_r$ is estimated and the free indices i and k run over all data points.

Combining the above formulas, the optimal estimation of the component *reg* can be written as:

$$\tilde{g}_{reg}(p_j) = \overline{w}_j \cdot \overline{g} = \overline{R}_{reg,j} \cdot (\mathbf{R}_{reg} + \alpha^{-1}\mathbf{R}_{loc})^{-1} \cdot \overline{g} \qquad (3)$$

We will show that Eq. 3 is equivalent to approximation of the measured field using two sets of causative sources situated at different depths. Consider the same gravity anomaly measured at points $p_k = \{R_z \phi_k \lambda_k\}$, where R_z is the Earth's radius, and consider two sets of elementary sources, situated below the measurement points at depths h_{reg} and h_{loc}, so that their coordinates are $\{R_z - h_{reg}, \phi_k, \lambda_k\}$ and $\{R_z - h_{loc}, \phi_k, \lambda_k\}$. Let the masses of two sources be linearly dependent, i.e. if m_k is the mass of elementary sources situated at the depth h_{reg} below point p_k, then the mass of the source situated at the depth h_{loc} below the same point is m_k/β. Any gravity anomaly measured at points p_j of the Earth's surface can be presented as a sum of effects of these two systems of sources:

$$g(p_j) = \sum_k m_k \{G_{reg}(h_{reg}, r_{jk}) + \beta^{-1} G_{loc}(h_{loc}, r_{jk})\} \qquad (4)$$

where G_{reg} and G_{loc} are the normalized (i.e. $G(h,0) = 1$) gravity effects of elementary sources situated at the depth h_{reg} and h_{loc} (e.g. point masses, dipole, etc.); and r_{jk} is again the distance between points p_j and p_k along the Earth's surface. Vector $\overline{m} = \{m_k\}$ can be found by solving the system of linear Eq. 4 and the regional component of the gravity field can be calculated from the equation:

$$\tilde{g}_{reg}(p_j) = \sum_k m_k G_{reg}(h_{reg}, r_{jk}) \qquad (5)$$

Introducing matrix notations $\mathbf{G}_{reg} = \{G_{reg}(h_{reg}, r_{jk})\}$ and $\mathbf{G}_{loc} = \{G_{loc}(h_{loc}, r_{jk})\}$ and replacing m_k in Eq. 5 by its expression that follows from Eq. 4, one arrives at the following formula:

$$\tilde{g}_{reg}(p_j) = \overline{G}_{reg,j} \cdot \overline{m} = \overline{G}_{reg,j} \cdot (\mathbf{G}_{reg} + \beta^{-1} \cdot \mathbf{G}_{loc})^{-1} \overline{g} \qquad (6)$$

which is identical to Eq. 3 if the functions G_{reg} and G_{loc} are chosen such that $G_{reg}(h_{reg}, r) = R_{reg}(r)$ and $G_{loc}(h_{loc}, r) = R_{loc}(r)$, and $\beta = \alpha = \sigma^2_{reg}/\sigma^2_{loc}$. Hence, the procedure of field separation by means of the equivalent source approximation (Eqs. 4 and 5) is equivalent to the Kolmogorov–Wiener optimal filtration (Eqs. 1–3).

This approach can be extended to the case of measurements on irregular topography and to the case of several separable components. The advantage of using the causative source approach is that once the values of masses m_k are found, the data reduction to any surface, calculation of directional derivatives and other field transformations become trivial.

The field separation algorithm includes the following steps: (1) calculation of the auto-correlation function of the measured anomaly; (2) the approximation of the calculated auto-correlation function by a linear combination of the functions G_{reg} and G_{loc} and the estimation of parameters h_{reg}, h_{loc} and β; (3) the solution of Eq. 4 for the masses m_k; (4) the calculation of field components.

To estimate the auto-correlation function under the assumption of field isotropy we used the formula:

$$\tilde{R}(k\Delta) = \frac{1}{n_k} \sum_{i,j} g(p_i) g(p_i) \qquad (7)$$

where the summation is performed over the points p_i and p_j such that the distance between them along the Earth's surface r_{ij} satisfies the inequality $k\Delta \leq r_{ij} \leq (k+1)\Delta$. Here Δ is an averaging parameter and n_k is a number of points in the kth interval. It was proven by Kolmogorov [29] that

---

←
Fig. A2. Spatial distribution of absolute values of discrepancy between MODEC 1994 data and KMS 1998 gravity field model along the MODEC tracks. Absolute values of discrepancy given by colors. Below is histogram of discrepancy distribution.

Eq. 7 provides a well-grounded unbiased estimate of the auto-correlation function averaged over the intervals $[k\Delta,(k+1)\Delta]$.

References

[1] T.J. Fitch, Plate convergence, trunscurrent faulting and internal deformation adjacent to southeast Asia and western Pacific, J. Geophys. Res. 77 (1972) 4432–4460.

[2] W. Hamilton, Tectonics of the Indonesian region, USGS Prof. Pap. 1078 (1979) 345 pp.

[3] E.A. Silver, J.C. Moore, The Molucca Sea collision zone, Indonesia, J. Geophys. Res. 83 (1978) 1681–1691.

[4] R.K. Cardwell, B.L. Isacks, D.E. Karig, The spatial distribution of earthquakes, focal mechanism solutions, and subducted lithosphere in the Philippine and north-eastern Indonesian Islands, in: D.E. Hayes (Ed.), The Tectonic and Geologic Evolution of Southeast Asian Seas and Islands, Part I, Geophys. Monogr. Ser. 23 (1980) 1–35.

[5] R. Hall, Plate boundary evolution in the Halmahera region, Indonesia, Tectonophysics 144 (1987) 337–352.

[6] R. McCaffrey, E.A. Silver, R.W. Raitt, Crustal structure of the Molucca Sea collision zone Indonesia, in: D.E. Hayes (Ed.), The Tectonic and Geologic Evolution of Southeast Asian Seas and Islands, Part I, Geophys. Monogr. Ser. 23 (1980) 161–177.

[7] G.F. Moore, E.A. Silver, Collision processes in the northern Molucca Sea, in: D.E. Hayes (Ed.), The Tectonic and Geologic Evolution of Southeast Asian Seas and Islands, Part II, Geophys. Monogr. Ser. 27 (1983) 360–371.

[8] G.F. Moore, C.A. Evans, J.W. Hawkins, D. Kadarisman, Geology of the Talaud Islands, Molucca Sea collision zone, Northeast Indonesia, J. Struct. Geol. 3 (1981) 467–475.

[9] C.A. Evans, J.W. Hawkins, G.F. Moore, Petrology and geochemistry of ophiolitic and associated volcanic rocks on the Talaud island, Molucca Sea collision zone, Northeast Indonesia, in: T.W.C. Hilde, S. Uyeda (Eds.), Geodynamics of the Western Pacific-Indonesian region, Geodyn. Ser. 11 (1983) 159–172.

[10] A.G. Bader, M. Pubellier, C. Rangin, C. Deplus, R. Louat, Active slivering of oceanic crust along the Molucca Ridge (Indonesia-Philippines), Tectonics 18 (1999) 606–620.

[11] C. Rangin, D. Dahrin, R. Quebral, and the Modec Scientific Party, Collision and strike-slip faulting in the Northern Molucca Sea (Philippines and Indonesia): preliminary results of a morphotectonic study, in: R. Hall, D. Blundel (Eds.), The Tectonic Evolution of Southeast Asia, Geol. Soc. Spec. Publ. 106 (1996) 29–46.

[12] M. Pubellier, A.G. Bader, B. Deffontaines, C. Rangin, R. Quebral, Upper plate deformation induced by subduction of a volcanic arc: the Snellius Plateau (Molucca Sea, Indonesia and Mindanao Philippines), Tectonophysics 304 (1999) 345–368.

[13] S.E. Lallemand, M. Popoff, J.P. Cadet, A.G. Bader, M. Pubellier, C. Rangin, B. Deffontaines, Genetic relations between the central and southern Philippine Trench and the Sangihe Trench, J. Geophys. Res. 103 (1998) 933–950.

[14] V.M. Gordin, B.O. Mikhailov, V.O. Mikhailov, Physical aspects of anomalous fields approximation and filtration, Izvestiya, Phys. Solid Earth 16 (1980) 52–61.

[15] V. Mikhailov, A. Galdeano, M. Diament, A. Gvishiani, S. Agayan, S. Bogoutdinov, E. Graeva, P. Sailhac, Application of artificial intelligence for Euler solutions clustering, Geophysics 68 (2003) 168–180.

[16] O.B. Andersen, P. Knudsen, Global marine gravity field from the ERS-1 and Geosat geodetic mission altimetry, J. Geophys. Res. 103 (1998) 8129–8137.

[17] W.H.F. Smith, D.T. Sandwell, Global Sea floor topography from satellite altimetry and ship depth soundings, Science 277 (1997) 1956–1962.

[18] R.L. Parker, The rapid calculation of potential anomalies, Geophys. J. R. Astron. Soc. 31 (1972) 447–455.

[19] V.M. Gordin, E.N. Rose, Optimal interpolation of the geomagnetic measurements and singular approximations, Geomagn. Aeron. 24 (1985) 124–128.

[20] M.E. Artemjev, T.M. Babaeva, V.O. Mikhailov, I.E. Voydetsky, Identification of mantle and lithospheric components of the gravity field by isostatic gravity anomalies, Mar. Geophys. Res. 7 (1984) 129–148.

[21] A. Gvishiani, J.O. Dubois, Artificial Intelligence and Dynamic Systems for Geophysical Applications, Springer, Berlin, 2002, 385 pp.

[22] D.T. Thompson, EULDPH: A new technique for making computer-assisted depth estimates from magnetic data, Geophysics 47 (1982) 31–37.

[23] A.G. Bader, M. Pubellier, Forearc deformation and tectonic significance of the ultramafic Molucca central ridge, Talaud island (Indonesia), Island Arc 9 (2000) 653–663.

[24] E.R. Engdahl, R.D. Van der Hilst, R.P. Bulland, Global teleseismic earthquake relocation with improved travel times and procedures for depth determination, Bull. Seismol. Soc. Am. 88 (1998) 722–743.

[25] C. De Mets, R.G. Gordon, D.F. Argus, S. Stein, Current plate motions, Geophys. J. Int. 101 (1990) 425–478.

[26] T. Seno, S. Stein, A.E. Gripp, A model for the motion of the Philippine Sea Plate consistent with NUVEL-1 and geological data, J. Geophys. Res. 98 (1993) 17941–17948.

[27] D.T. Sandwell, W.H.F. Smith, Marine gravity from Geosat and ERS 1 satellite altimetry, J. Geophys. Res. 102 (1997) 10039–10054.

[28] J.D. Fairhead, C.M. Green, High resolution satellite derived gravity is now a reality, XXVII EGS General Assembly, Nice, France, Geophys. Res. Abstr. 4 (2002) EGS02-A-06823 (CD-ROM).

[29] A.N. Kolmogorov, Interpolation and extrapolation of the stationary random time series, Izv. Acad. Sci. USSR, mathematical series N5 (1941) 3–14.

[30] N. Wiener, The Interpolation, Extrapolation and Smoothing of the Stationary Time Series with Engineering Applications, MIT Press, Cambridge, MA, 1949, 326 pp.